

Accepted Manuscript

Title: Molten pool behavior in the tandem submerged arc welding process

Author: Dae-Won Cho Degala Venkata Kiran Woo-Hyun
Song Suck-Joo Na



PII: S0924-0136(14)00164-2
DOI: <http://dx.doi.org/doi:10.1016/j.jmatprotec.2014.04.032>
Reference: PROTEC 13984

To appear in: *Journal of Materials Processing Technology*

Received date: 11-2-2014
Revised date: 24-4-2014
Accepted date: 27-4-2014

Please cite this article as: Cho, D.-W., Kiran, D.V., Song, W.-H., Na, S.-J., Molten pool behavior in the tandem submerged arc welding process, *Journal of Materials Processing Technology* (2014), <http://dx.doi.org/10.1016/j.jmatprotec.2014.04.032>

This is a PDF file of an unedited manuscript that has been accepted for publication. As a service to our customers we are providing this early version of the manuscript. The manuscript will undergo copyediting, typesetting, and review of the resulting proof before it is published in its final form. Please note that during the production process errors may be discovered which could affect the content, and all legal disclaimers that apply to the journal pertain.

Molten pool behavior in the tandem submerged arc welding process

Dae-Won Cho ^a, Degala Venkata Kiran ^b, Woo-Hyun Song ^c, Suck-Joo Na ^b

^aIndustrial Technology Institute, Hyundai Heavy Industries, Ulsan, Republic of Korea

^bDepartment of Mechanical Engineering, KAIST, Daejeon, Republic of Korea

^cTechnical Research Laboratories, POSCO, Pohang, Republic of Korea

Abstract

A three-dimensional numerical heat transfer and fluid flow model are developed to examine the temperature profiles, velocity fields, weld pool shape and size in a two-wire tandem submerged arc welding process. The model solves the equations of the conservation of mass, momentum, and energy along with the volume of fluid method. The volume of fluid method is used to track the shape of the free surface. Further, a novel scheme is proposed to handle the arc interaction and its influence on the molten droplet transfer direction. Using the computational fluid dynamics simulations, it is found that the droplet movement and arc forces from the leading electrode heavily affect the molten pool flow patterns and the resultant bead shapes, even though the same heat inputs are applied. The computed weld width and penetration are in fair agreement with the corresponding experimental results.

Keywords

Submerged arc welding, Tandem welding, Computational fluid dynamics, Volume of fluid, Molten pool flow

1. Introduction

The two-wire tandem submerged arc welding (SAW-T) process has been considered as a potential replacement to a single-wire SAW process, due to the high deposition capabilities of former. Detailed understanding of the temperature and fluid flow is a prerequisite for the successful application of any welding process because they directly influence the weld pool dimensions, the cooling rates, and the resulting microstructure and mechanical properties of the weld. The presence of the welding arc and small weld pool with sharp temperature gradients make the physical measurement of temperature and velocity fields a very difficult task. It is even more complex in the SAW-T process due to the presence of a heavy granular flux, multiple arcs and their interaction, and the simultaneous deposition of molten metal from two electrode wires. Therefore, numerical modeling is a practical recourse and provides a better understanding of the weld pool temperature and velocity profiles in a more effective and economical way.

To date, a significant amount of work has been reported on the numerical modeling of deposition welding processes, such as gas metal arc welding (GMAW) and submerged arc welding (SAW), while the similar studies on the SAW-T process are scarce. Pardo and Weckman (1989), and Kumar and Bhaduri (1994) modeled the GMAW process considering the heat transfer from the welding arc by a Gaussian distributed surface heat source, and the heat transfer from superheated molten electrode droplets was simulated by surface heat source and cylindrical volumetric heat source, respectively. Mahapatra et al. (2006) used an element deactivation and activation technique to simulate the deposition of the electrode molten metal in the SAW process. Kiran et al. (2010) and Kiran et al. (2011) simulated SAW-T process by considering heat transfer from the leading and trailing arcs with two independent double ellipsoidal volumetric heat sources. All these described models are the conduction-based models, and hence they fail to consider the convection phenomenon inside the weld pool.

Considering the importance of the weld pool convection in deposition welding processes, numerous researchers have attempted to analyze the heat transfer and fluid flow in the weld pool. Tsao and Wu (1988) developed a 2D stationary weld pool convection model by assuming a flat weld pool surface. Many researchers used a boundary fitted coordinate system in conjunction with finite difference techniques to calculate the temperature and fluid flow considering the deformation of the weld pool surface. Kim and Na (1995) calculated the free surface profile by minimizing the total free surface energy considering the addition of a filler. Furthermore, Kim et al. (2003) found out that heat and fluid flow distribution is also strongly influenced by the additional heat transfer by the molten electrode

droplets and their impact on the weld pool free surface. The heat supplied by the molten droplets to the weld pool was modeled by an internal heat generation term. Ushio and Wu (1997) considered the impact of the droplets using a constant applied force term. Jaidi et al. (2001) used a cylindrical volumetric heat source to describe droplet effects. However, all these models based on this transport phenomenon cannot explain the dynamic nature of the weld pool.

In computational fluid dynamics, the volume of fluid (VOF) technique calculates the accurate shape and motion of free fluid surfaces. Wang and Tsai (2001) developed a numerical model employing the VOF technique to simulate weld pool fluid flow resulting from the dynamic impinging of droplets in a spot GMAW process. Using the VOF technique, Cao et al. (2004) calculated a 3D transient molten pool fluid for a linearly moving GMAW process. It was reported that among all the forces, the metal droplet impact was the primary force responsible for penetration. Cho et al. (2013a) successfully predicted the unstable molten pool flow patterns, such as humping and overflow, in V-groove positional GMAW using the VOF technique. The dimensions of the surface heat source were measured from CCD images of the arc using the Abel inversion method. Cho and Na (2009) and Cho et al. (2010) described the dynamic fluid flow in complex welding processes like GMA-laser hybrid welding using the VOF technique. Cho et al. (2013b) measured arc plasma distributions of direct current (DC) and alternating current (AC) single electrode SAW, and then applied the results to CFD simulations so that several arc models, such as, arc heat source, arc pressure and electromagnetic force (EMF) models, could be validated.

In summary, although numerical models are available to understand the heat and fluid flow in single wire GMAW and SAW processes, no attempts have been made until now to address the same issues in the SAW-T process. This paper proposes a 3D transient heat transfer and fluid flow model for the SAW-T process using the commercial CFD software, Flow-3D. The novelty of this work is that the heat transfer from the two welding arcs is considered with two independent Gaussian distributed heat sources. Next the dynamic impingement of the molten drops corresponding to the two electrode wires on the weld pool is considered. Further, the interaction between the two arcs and its influence on the molten metal droplet flight is studied. Finally the computed weld pool dimensions are validated with corresponding experimental results.

2. Theoretical Formulation

2.1 Material shape and mesh size

This study conducts four experiments for the SAW-T process, and describes the molten pool dynamics. Fig. 1 shows a schematic sketch of the V-groove materials and the position of the electrodes in the 3D x-y-z coordinate system. Cho et al. (2013b) used at least four meshes for the droplet diameter. Thus, this paper used a mesh density of as 0.3mm/mesh to describe the molten pool flow and droplet movement accurately. Welding starts at 1.5cm in the x-direction.

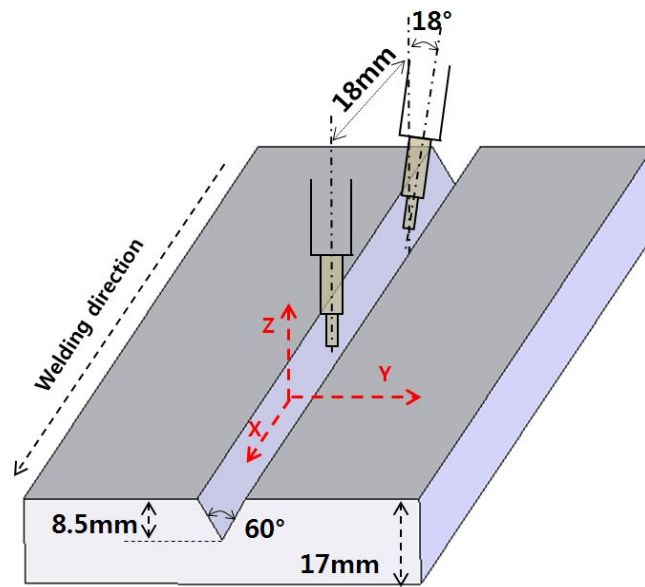


Fig. 1 Schematic sketch of experimental setup

2.2 Governing equations

In the commercial software Flow-3D, Navier–Stokes, energy conservation and VOF equations are involved; therefore, these equations can be solved by Flow-3D. The materials properties and variables are provided in Table 1.

- Momentum equation:

$$\rho \frac{\partial \vec{V}}{\partial t} + \rho(\vec{V} \cdot \nabla)\vec{V} = -\nabla p + \nabla^2 \vec{V} + f_b \quad (1)$$

- Continuity equation -

$$\nabla \cdot \vec{V} = 0 \quad (2)$$

- Energy equation -

$$\frac{\partial h}{\partial t} + (\vec{V} \cdot \nabla)h = \frac{1}{\rho} \nabla \cdot (k \nabla T), \quad \text{where} \quad h = C_p T + f(T) L_f \quad (3)$$

$$f(T) = \begin{cases} 0 & (T \leq T_s) \\ \frac{T - T_s}{T_l - T_s} & (T_s < T < T_l) \\ 1 & (T_l \leq T) \end{cases} \quad (4)$$

- VOF equation -

$$\frac{dF}{dt} = \frac{\partial F}{\partial t} + (\vec{V} \cdot \nabla)F = 0 \quad (5)$$

Table 1 Properties and constants used in simulations

Accepted Manuscript

Symbol	Nomenclature	Symbol	Nomenclature
ρ	Density, (solid:7.8, liquid:6.9, g/cm ³)	σ_{FT}	Front effective radius of the trailing arc in x-direction
\vec{V}	Velocity vector	σ_{AL}	Mean value of σ_{RL} and σ_{FL}
f_b	Body force	σ_{AT}	Mean value of σ_{RT} and σ_{FT}
h	Enthalpy	k_{yL}, k_{yT}	Weighting factor, 0.65, 0.85
F	Fraction of fluid	T_o	Room temperature, 298K
k	Thermal conductivity	η_s	Slag efficiency of SAW
\vec{n}	Normal vector to free surface	\dot{m}_f	Flux consumption (g/s)
q_a	Heat input from arc plasma	C_{pf}	Specific heat of flux (s-777MHX), 1.01J/g
q_{slag_input}	Heat transfer from slag to molten pool	$T_{m,flux}$	Melting temperature of flux (s-777MHX), 1273K
q_{slag_loss}	Heat transfer from molten pool to slag	V_{L_rms}	RMS value of V_L
q_s	Heat input from slag	I_{L_rms}	RMS value of I_L
η_{SAW}	Thermal efficiency of SAW, 0.95	V_{L_rms}	RMS value of V_T
q_d	Heat input from droplet	I_{L_rms}	RMS value of I_L
p_A	Arc pressure	R_{bL}	Outer boundary of slag for the leading arc
R_c	Radius of the surface curvature	R_{aL}	Inner boundary of slag for the leading arc
γ	Surface tension	R_{bT}	Outer boundary of slag for the trailing arc
q_{aL}	Heat input from the leading arc	R_{aT}	Inner boundary of slag for the trailing arc
q_{aT}	Heat input from the trailing arc	μ_0	Permeability of vacuum, 1.26x10 ⁶ H/m
η_a	Arc efficiency of SAW	μ_m	Material permeability, 1.26x10 ⁶ H/m
V_L, I_L	Voltage and current of the leading electrode	J_{zL}, J_{zT}	Vertical component of the current density for leading and trailing arcs
V_T, I_T	Voltage and current of the trailing electrode	J_{rL}, J_{rT}	Radial component of the current density for leading and trailing arcs
x_0, y_0	Location of the leading arc center in x and y directions	$B_{\theta L}, B_{\theta T}$	Angular component of the magnetic field for leading and trailing arcs
x_1, y_1	Location of the leading arc center in x and y directions	J_0	First kind of Bessel function of zero order
q_{aL}	Heat input from the leading arc	J_1	First kind of Bessel function of first order
q_{aT}	Heat input from the trailing arc	c	Distance between top free surface and bottom
η_a	Arc efficiency of SAW	z	Distance from top free surface
σ_{RL}	Rear effective radius of the leading arc in x-direction	l_L, l_T	Arc length of leading and trailing arcs
σ_{FL}	Front effective radius of the leading arc in x-direction	β_n^{ij}	Coefficients of effective radius model
σ_{RT}	Rear effective radius of the trailing arc in x-direction	d	Distance between leading and trailing electrodes, 18mm

3.2 Boundary conditions

Because flux and slag cover the overall weld bead in the SAW-T process, there is no heat loss from the convection, radiation and evaporation on the weld pool surface; moreover, the heat can be transferred between the molten pool boundary and slag. Cho et al. (2013b) considered the heat input and heat loss from the molten slag and then applied the results to the energy boundary conditions in equation (6).

$$k \frac{\partial T}{\partial n} = q_a + q_{slag_input} - q_{slag_loss} = q_a + q_s \quad (6)$$

Shome (2007) adopted a thermal efficiency of 0.95 in SAW; therefore, this study also uses a total thermal efficiency of 0.95 in equation (7).

$$\eta_{SAW} = \frac{q_a + q_d + q_s}{VI} \approx 0.95 \quad (7)$$

Equation (8) is applied for the pressure boundary on the free surface.

$$p = p_A + \frac{\gamma}{R_c}, \quad (8)$$

3.2.1 Arc interaction model

Kiran et al. (2014) found that the arc displacement as well as the effective radius of arc plasma can be changed in the SAW-T process. From equations (9) and (10), it is possible to expect that a higher current arc plasma is more stable than a lower current arc plasma. Additionally, a lower current arc plasma can be shifted more due to the arc interaction effect.

$$X_L = C_1 \left(\frac{I_T}{I_L} \right) \left(\frac{l_L^2}{d} \right) \quad (9) \quad X_T = C_2 \left(\frac{I_L}{I_T} \right) \left(\frac{l_T^2}{d} \right) \quad (10)$$

Kiran et al. (2014) also proposed the effective radius of arc model as shown in equation (11), where the welding current and voltage values are used.

$$\begin{aligned} \sigma_{ij} = & \beta_0^{ij} + \beta_1^{ij} * I_j + \beta_2^{ij} * V_j + \beta_3^{ij} * X_j + \beta_4^{ij} * I_j^2 + \beta_5^{ij} * V_j^2 + \beta_6^{ij} * X_j^2 \\ & + \beta_7^{ij} * (I_j * V_j) + \beta_8^{ij} * (V_j * X_j) + \beta_9^{ij} * (I_j * X_j) \end{aligned} \quad (11)$$

3.2.2 Arc heat source model

With the linear regression model, trapezoidal square wave signals (voltage and current) are used in the simulation as shown in Fig. 2 and Fig. 3. Cho et al. (2013b) described the Gaussian asymmetric arc heat source model, which contains different temperature distributions for the front and rear parts; therefore, this paper adopts the resultant effective radius to describe the Gaussian asymmetric arc heat source model. The frequency of the AC welding signal is 60Hz. Equations (12) and (13) describe the arc heat source models for the leading and trailing arc plasmas.

$$\text{if } x \leq x_0 \text{ then, } q_{aL}(x, y) = \frac{\eta_a V_L I_L}{2\pi\sigma_{AL}^2} \exp\left(-\frac{(x-x_0)^2}{2\sigma_{RL}^2} - \frac{y^2}{2\sigma_{AL}^2}\right) \quad (12), \text{ where } \sigma_{AL} = k_{yL}(\sigma_{FL} + \sigma_{RL})/2.$$

$$\text{if } x > x_0 \text{ then, } q_{aL}(x, y) = \frac{\eta_a V_L I_L}{2\pi\sigma_{AL}^2} \exp\left(-\frac{(x-x_0)^2}{2\sigma_{FL}^2} - \frac{y^2}{2\sigma_{AL}^2}\right)$$

$$\text{if } x \leq x_1 \text{ then, } q_{aT}(x, y) = \frac{\eta_a V_T I_T}{2\pi\sigma_{AT}^2} \exp\left(-\frac{(x-x_0)^2}{2\sigma_{RT}^2} - \frac{y^2}{2\sigma_{AT}^2}\right) \quad (13), \text{ where } \sigma_{AT} = k_{yT}(\sigma_{FT} + \sigma_{RT})/2.$$

$$\text{if } x > x_1 \text{ then, } q_{aT}(x, y) = \frac{\eta_a V_T I_T}{2\pi\sigma_{AT}^2} \exp\left(-\frac{(x-x_0)^2}{2\sigma_{FT}^2} - \frac{y^2}{2\sigma_{AT}^2}\right)$$

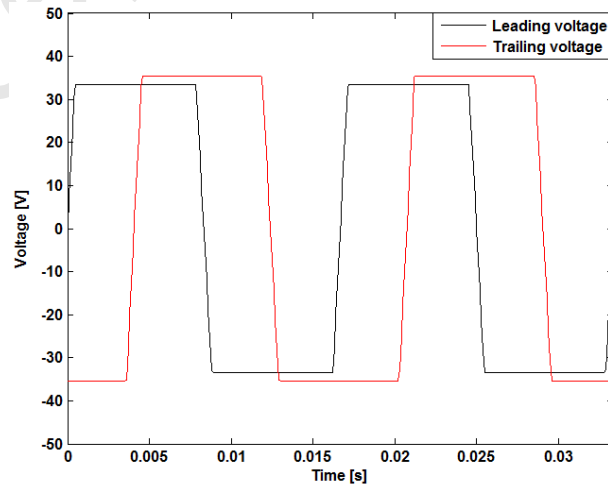


Fig. 2 Voltage values for all cases in the simulations

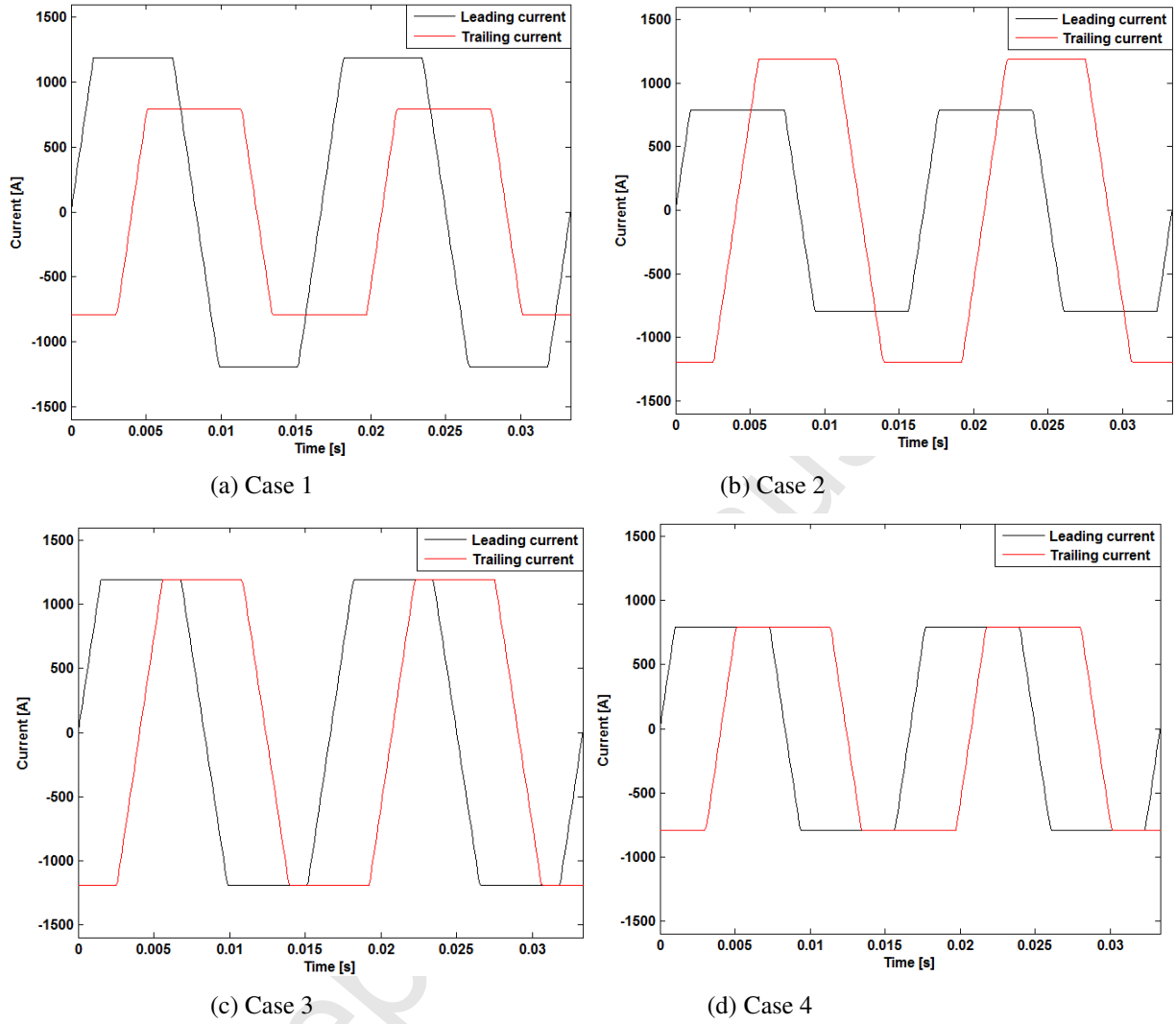


Fig. 3 Current values in the simulations

3.2.3 Slag heat source model

Cho et al. (2013b) assumed that the molten slag is generated by some portion of the arc heat energy, and the molten slag acts as a heat source to the material surface. This paper also adopts the slag heat efficiency using the flux consumption.

$$\eta_s = \frac{\dot{m}_f C_{pf} (T_{m,flux} - T_o)}{V_{L_rms} I_{L_rms} + V_{T_rms} I_{T_rms}} \quad (14)$$

This paper uses the elliptically ring-shaped slag heat source model as expressed in equations (12) to (15).

$$\begin{aligned} \text{if } x \leq x_0, r_{eL} &= \sqrt{(x-x_0)^2 \left(\frac{\sigma_{AL}}{\sigma_{RL}} \right)^2 + (y-y_0)^2} \\ \text{if } x > x_0, r_{eL} &= \sqrt{(x-x_0)^2 \left(\frac{\sigma_{AL}}{\sigma_{FL}} \right)^2 + (y-y_0)^2} \end{aligned} \quad (15)$$

$$\text{if } R_{aL} < r_{eL} \leq R_{bL} \text{ then, } q_s = \frac{\eta_s V_L I_L}{\pi(R_{bL}^2 - R_{aL}^2)} \quad (16), \text{ where } R_{aL} = 3\sigma_{AL}, R_{bL} = R_{aL} + 3.0\text{mm}.$$

$$\begin{aligned} \text{if } x \leq x_1, r_{eT} &= \sqrt{(x-x_0)^2 \left(\frac{\sigma_{AT}}{\sigma_{RT}} \right)^2 + (y-y_0)^2} \\ \text{if } x > x_1, r_{eT} &= \sqrt{(x-x_0)^2 \left(\frac{\sigma_{AT}}{\sigma_{FT}} \right)^2 + (y-y_0)^2} \end{aligned} \quad (17),$$

$$\text{if } R_{aT} < r_{eT} \leq R_{bT} \text{ then, } q_s = \frac{\eta_s V_T I_T}{\pi(R_{bT}^2 - R_{aT}^2)} \quad (18), \text{ where } R_{aT} = 3\sigma_{AT}, R_{bT} = R_{aT} + 3.0\text{mm}.$$

3.2.4 Arc pressure model

Cho et al. (2013a) assumed that the distribution of arc pressure could be the same as in the arc heat flux model; therefore, the effective radius of the arc heat flux model can also be used in the arc pressure model.

$$\begin{aligned} \text{if } x \leq x_0 \text{ then, } P_{aL}(x, y) &= \frac{\mu_0 I_L^2}{4\pi^2 \sigma_{AL}^2} \exp\left(-\frac{(x-x_0)^2}{2\sigma_{RL}^2} - \frac{y^2}{2\sigma_{AL}^2}\right) \\ \text{if } x > x_0 \text{ then, } P_{aL}(x, y) &= \frac{\mu_0 I_L^2}{4\pi^2 \sigma_{AL}^2} \exp\left(-\frac{(x-x_0)^2}{2\sigma_{FL}^2} - \frac{y^2}{2\sigma_{AL}^2}\right) \end{aligned} \quad (19), \text{ where } \sigma_{AL} = k_{yL}(\sigma_{FL} + \sigma_{RL})/2$$

$$\begin{aligned} \text{if } x \leq x_1 \text{ then, } P_{aT}(x, y) &= \frac{\mu_0 I_T^2}{4\pi^2 \sigma_{AT}^2} \exp\left(-\frac{(x-x_0)^2}{2\sigma_{RT}^2} - \frac{y^2}{2\sigma_{AT}^2}\right) \\ \text{if } x > x_1 \text{ then, } P_{aT}(x, y) &= \frac{\mu_0 I_T^2}{4\pi^2 \sigma_{AT}^2} \exp\left(-\frac{(x-x_0)^2}{2\sigma_{FT}^2} - \frac{y^2}{2\sigma_{AT}^2}\right) \end{aligned} \quad (20), \text{ where } \sigma_{AT} = k_{yT}(\sigma_{FT} + \sigma_{RT})/2$$

3.3 Electromagnetic force

In the arc welding process, Kou and Sun (1985) found that the current density and self-induced magnetic field should be used to calculate the electromagnetic force (EMF) in the molten pool. In the molten slag of a high current SAW process, however, Cho et al. (2013b) ignored the current flow effect in the molten slag because the magnitude of the current in the molten slag is miniscule compared to the total current. Therefore, the EMF model is used only in molten pool fluid using the same effective arc radius as in the arc heat flux model.

$$J_{zL} = \frac{I_L}{2\pi} \int_0^{\infty} \lambda J_0(\lambda r) \exp(-\lambda^2 \sigma_{AL}^2 / 4d_a) \frac{\sinh[\lambda(c-z)]}{\sinh(\lambda c)} d\lambda \quad (21),$$

$$J_{rL} = \frac{I_L}{2\pi} \int_0^{\infty} \lambda J_1(\lambda r) \exp(-\lambda^2 \sigma_{AL}^2 / 4d_a) \frac{\cosh[\lambda(c-z)]}{\sinh(\lambda c)} d\lambda \quad (22),$$

$$B_{\theta L} = \frac{\mu_m I_L}{2\pi} \int_0^{\infty} J_1(\lambda r) \exp(-\lambda^2 \sigma_{AL}^2 / 4d_a) \frac{\sinh[\lambda(c-z)]}{\sinh(\lambda c)} d\lambda \quad (23),$$

$$F_{rL} = J_{zL} \times B_{\theta L} \quad (24), \quad F_{zL} = J_{rL} \times B_{\theta L} \quad (25),$$

$$J_{zT} = \frac{I_T}{2\pi} \int_0^{\infty} \lambda J_0(\lambda r) \exp(-\lambda^2 \sigma_{AT}^2 / 4d_a) \frac{\sinh[\lambda(c-z)]}{\sinh(\lambda c)} d\lambda \quad (26),$$

$$J_{rT} = \frac{I_T}{2\pi} \int_0^{\infty} \lambda J_1(\lambda r) \exp(-\lambda^2 \sigma_{AT}^2 / 4d_a) \frac{\cosh[\lambda(c-z)]}{\sinh(\lambda c)} d\lambda \quad (27),$$

$$B_{\theta T} = \frac{\mu_m I_T}{2\pi} \int_0^{\infty} J_1(\lambda r) \exp(-\lambda^2 \sigma_{AT}^2 / 4d_a) \frac{\sinh[\lambda(c-z)]}{\sinh(\lambda c)} d\lambda \quad (28),$$

$$F_{rT} = J_{zT} \times B_{\theta T} \quad (29), \quad F_{zT} = J_{rT} \times B_{\theta T} \quad (30)$$

3.4 Droplet model

Kiran et al. (2014) found that the molten droplet is directed to the arc center when it is just detached; moreover, the direction of the droplet could not be changed during the free flight. Fig. 4 shows the movement of the droplet flight during attraction and repulsion. This paper applies the molten droplet movement in the simulation. The droplet speed

is measured from the CCD arc images captured just outside the flux cavity in the tandem arc experiments performed for the welding conditions mentioned in Table 2 (Kiran et al., 2014). The CCD arc images are recorded at a sampling rate of 1 kHz. Initially, the droplet travel distance from the point of detachment at electrode tip to the weld pool is measured from the consecutive CCD arc images. Next, the droplet travel time is calculated as the ratio of the number of CCD arc images used to measure the droplet travel distance to the sampling rate. Finally, the droplet speed is calculated as the ratio of droplet travel distance to the corresponding travel time. For a given welding condition, the droplet speed is calculated for three times and the corresponding average value is reported in Table 2. Cho et al. (2013b) calculated the droplet efficiency by the wire feed rate and droplet size; therefore, this paper adopts the same method to obtain the droplet efficiency.

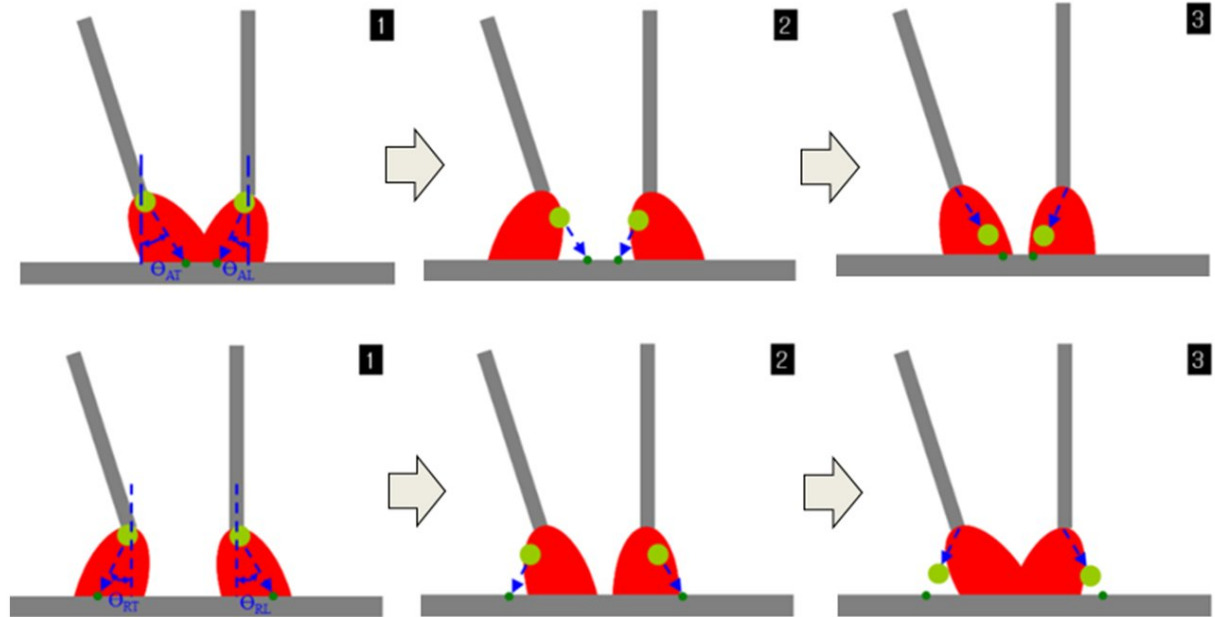


Fig. 4 Droplet flights due to the arc interaction effects in SAW-T process

3.6 Other welding models

Cho and Na (2009) applied the buoyancy force and the surface tension models, which do not include the effective radius of arc plasma. This study also used the same models.

4. Results and discussion

This paper conducts 4 different experiments and simulations, which are described in Table 2. The heat input per unit length (2.5 kJ/mm) are the same for all the cases; thus, it is possible to understand how the molten pool flows and the resultant bead shapes for the different welding conditions in the SAW-T process.

Table 2 Welding conditions

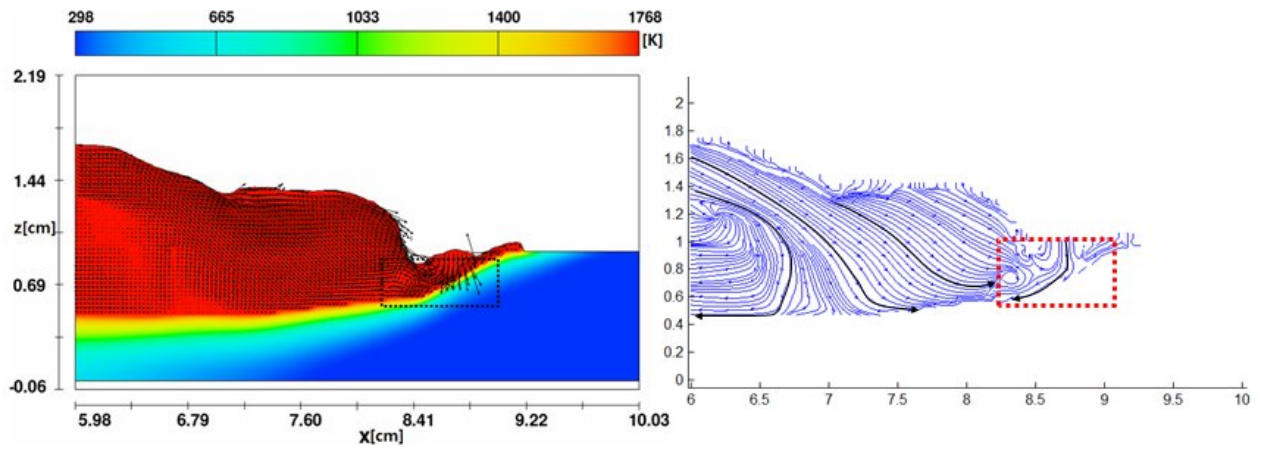
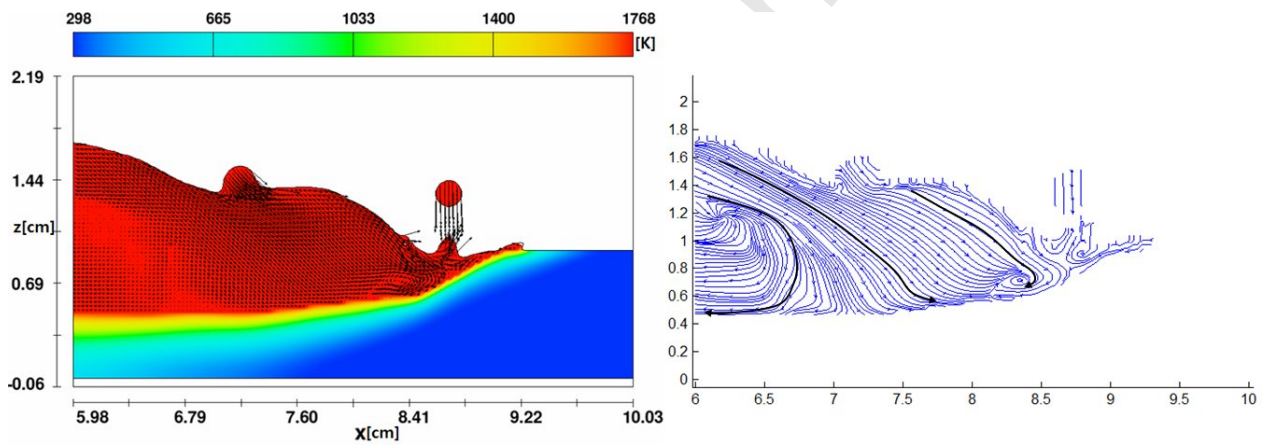
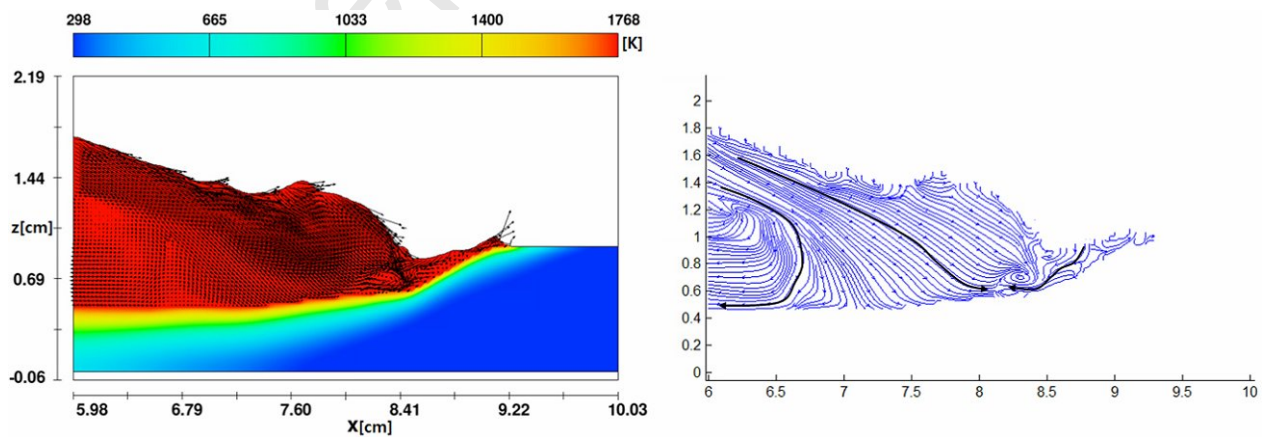
	Leading electrode ($\phi = 4.0mm$)				Trailing electrode ($\phi = 3.2mm$)				Welding speed (mm/s)	Total heat input (kJ/mm)
	Current (A)	Voltage (V)	Wire feed rate (m/min)	Droplet speed (mm/s)	Current (A)	Voltage (V)	Wire feed rate (m/min)	Droplet speed (mm/s)		
Case 1	1000A	32V	5.18	2000	700A	35V	1.8	1000	22.60	2.5
Case 2	700A	32V	3.21	1400	1000A	35V	2.77	1200	22.96	2.5
Case 3	1000A	32V	5.18	2000	1000A	35V	2.77	1200	26.80	2.5
Case 4	700A	32V	3.21	1400	700A	35V	1.8	1000	18.76	2.5

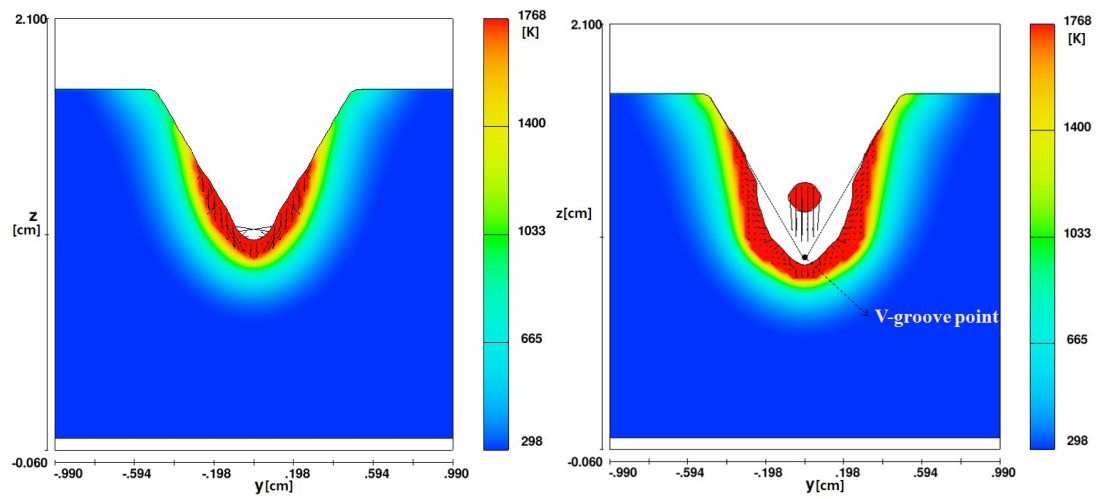
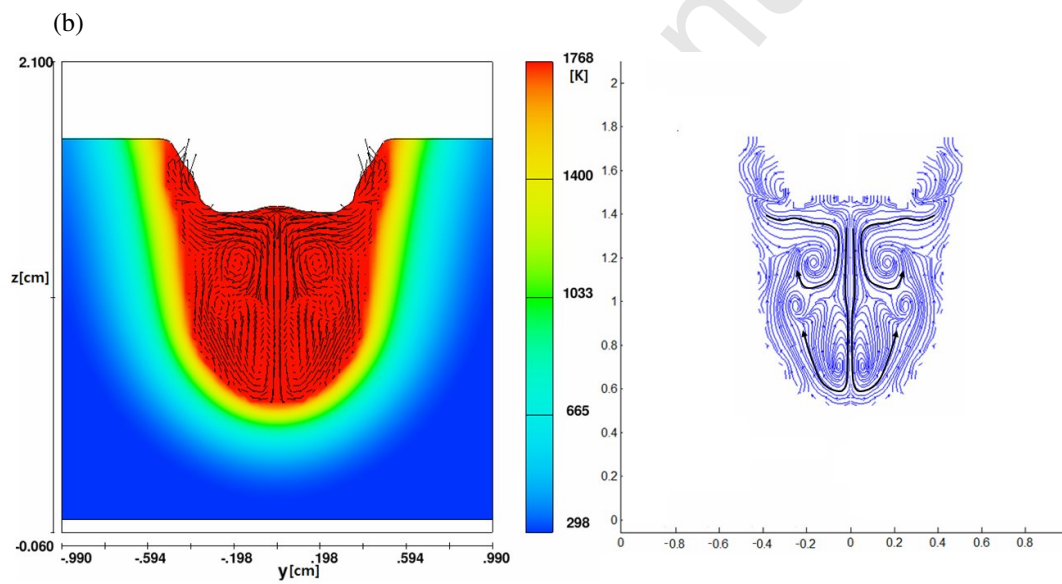
Kiran et al. (2014) found that when the absolute current value was higher, the arc stiffness increased; thus the arc tended to be fixed. However, when the absolute current value of the opposite electrode was higher, the arc stiffness decreased, so the arc tended to move backward or forward by the Lorentz force. Finally, the combination of current values from each electrode affected the arc center locations and droplet flights. For instance, the higher absolute current value can result in an increase in the wire feed rate, which can induce a frequent droplet impingement and a concentration of arc heat and arc forces.

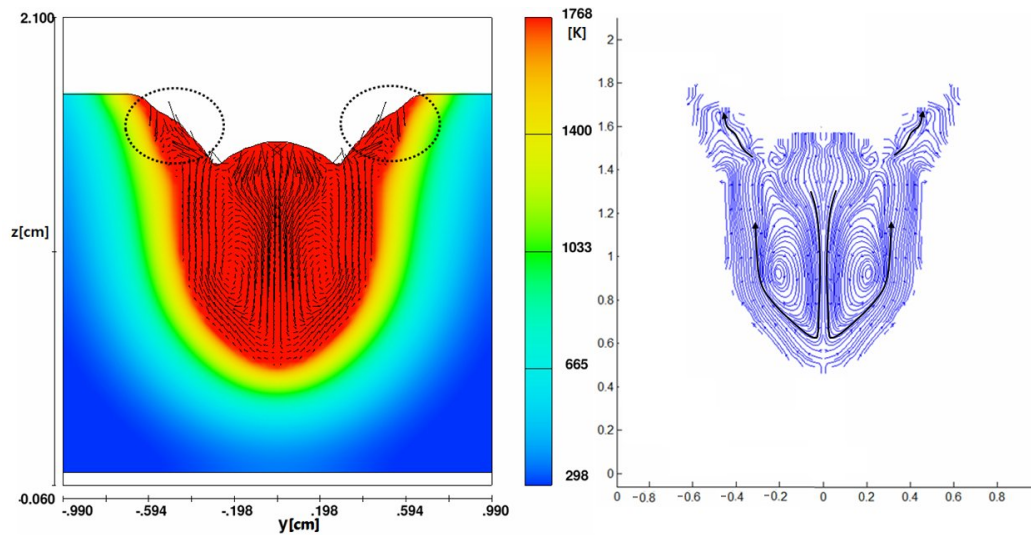
Using this principle, this paper performs CFD simulations and analyses the results. In Case 1, the RMS current values from the leading and trailing electrodes are 1000A and 700A, respectively, so the arc center displacement of the leading electrode is very small; moreover, the arc heat, arc force and droplet impingement can be focused under the leading electrode. Therefore, the volume of molten pool ahead of the leading electrode is very small because droplets do not fly ahead of the leading electrode as shown in Fig. 5. In the transverse section, droplets from the leading electrode impinge on the weld pool whose height is lower than the initial V-groove point; thus, the deep penetration can be formed as shown in Fig. 6(b). Moreover, the weld pool flows long after droplet impingement in the longitudinal section as shown in Figs. 5(a) to (c), so this can be another reason to make the deep penetration due to the dynamic convection heat transfer. Cho et al. (2013b) found that the voltage value significantly affects the arc

size and the resultant bead width; therefore, when the trailing electrode reaches the weld pool, the penetration is very slightly increased as shown in the dotted-circle of Fig. 6(d) while the bead width becomes wider because a higher voltage value can produce a large size of arc plasma.

Accepted Manuscript

(a) $t=3.130\text{s}$ (b) $t=3.134\text{s}$ (c) $t=3.138\text{s}$ **Fig. 5** Calculated temperature profiles and streamlines on the longitudinal cross-sections ($y=0\text{mm}$) in Case 1

(a) $t=1.193\text{s}$ (before droplet impingement)(b) $t=1.281\text{s}$ (c) $t=1.710\text{s}$

(d) $t=1.992s$ **Fig. 6** Calculated temperature profiles and streamlines on the transverse cross sections ($x=44.95\text{mm}$) of Case 1

In Case 2, the RMS current values from the leading and trailing electrodes are 700A and 1000A, where the current values are opposite to Case 1. Thus, the arc center displacement of the leading electrode due to the arc interaction is much bigger than that of Case 1. The droplets, arc heat, and arc forces from the leading electrode cannot be focused on a similar weld pool spot, but the droplets disperse forward or backward of welding direction and then form the volume of the molten pool ahead of the leading electrode as shown in Fig. 7. With these fluid behaviors, the molten pool can fill in the V-groove even though the leading electrode has not yet approached the spot. Consequently, the free surface location of z-direction during the droplet impingement is higher than the initial V-groove point, so the molten pool penetrates to a lesser degree than in Case 1 even though the momentum from the arc forces and droplet impingement affect the fluid flows in a transverse section as shown in Fig. 8(b). In the longitudinal section as shown in Fig. 7(c), the molten pool cannot flow downward sufficiently and circulate counterclockwise in a dotted-box; therefore, this molten fluid produces a bowl-shaped weld bead that shows a relatively shallow weld bead.

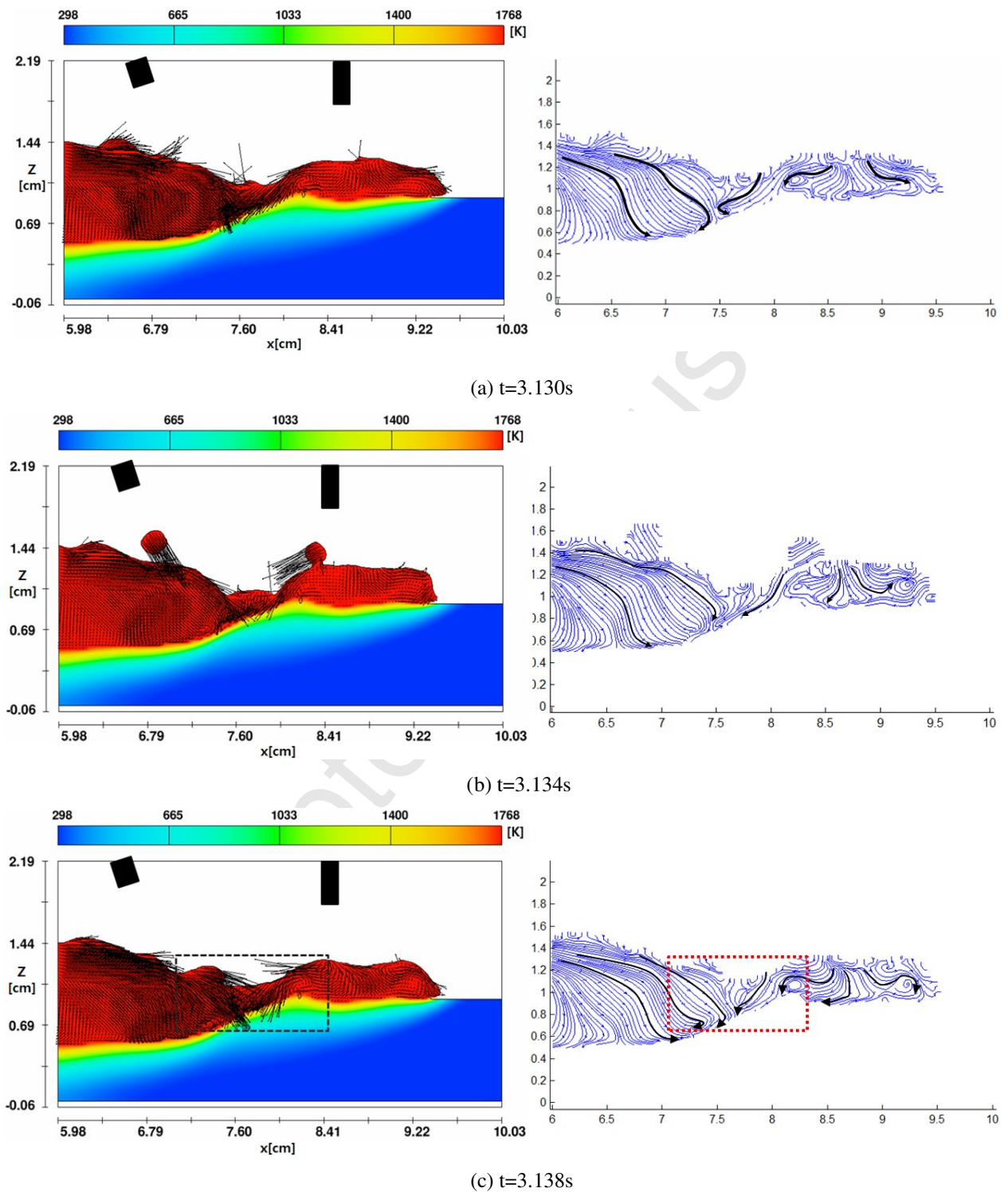
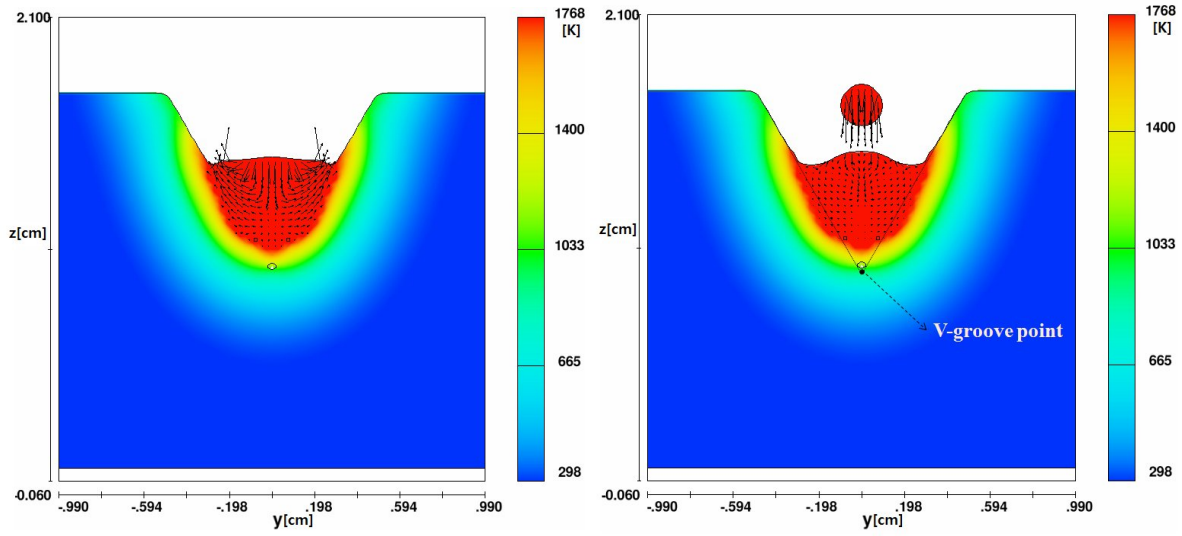
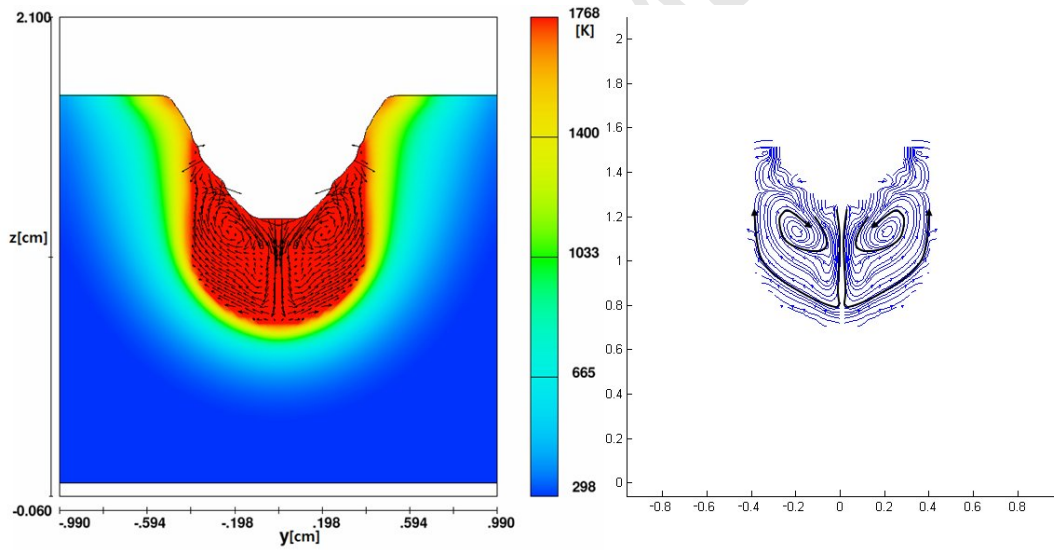


Fig. 7 Calculated temperature profiles and streamlines on the longitudinal cross-sections ($y=0\text{mm}$) of Case 2

(a) $t=1.257\text{s}$ (before droplet impingement)(b) $t=1.265\text{s}$ (c) $t=1.710\text{s}$

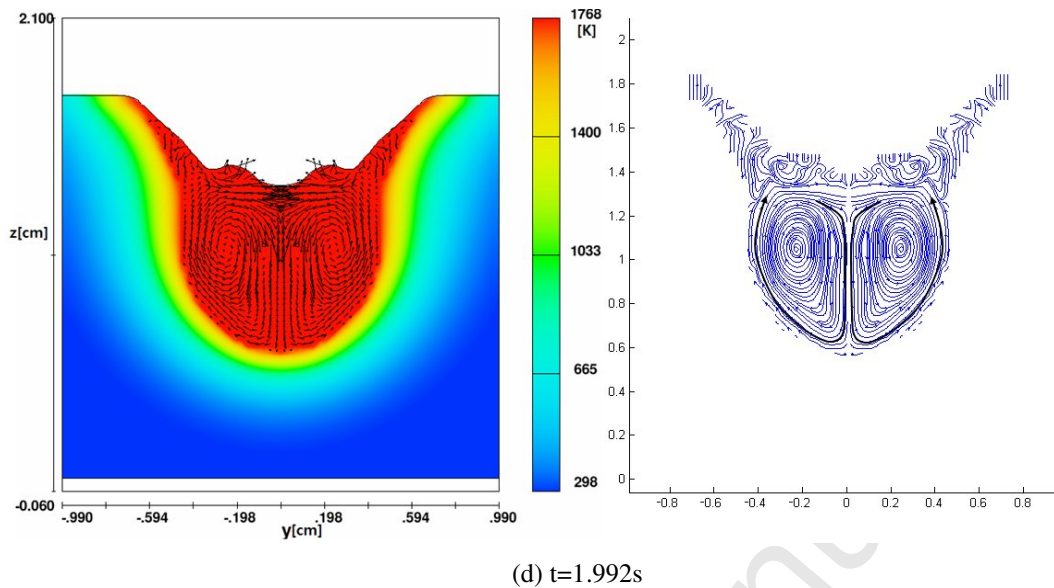
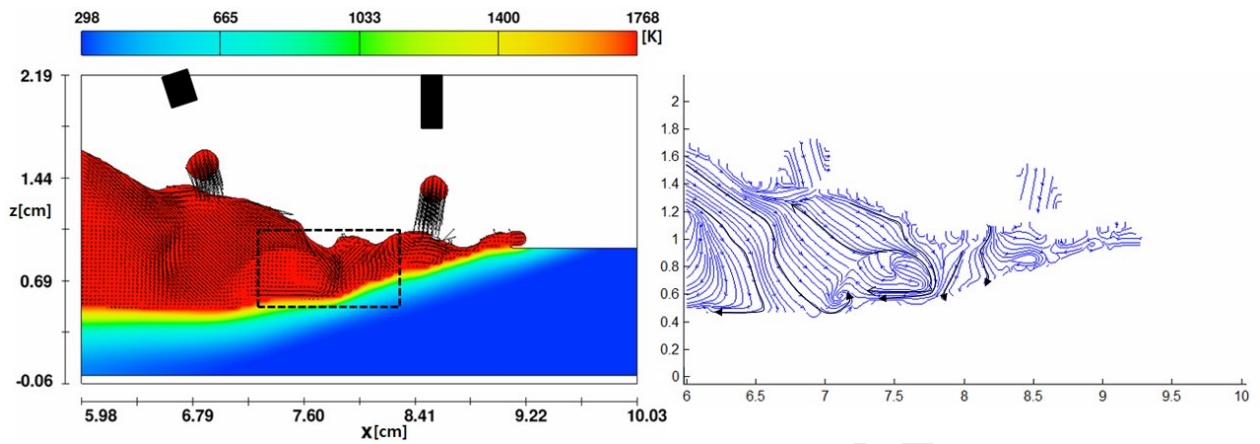
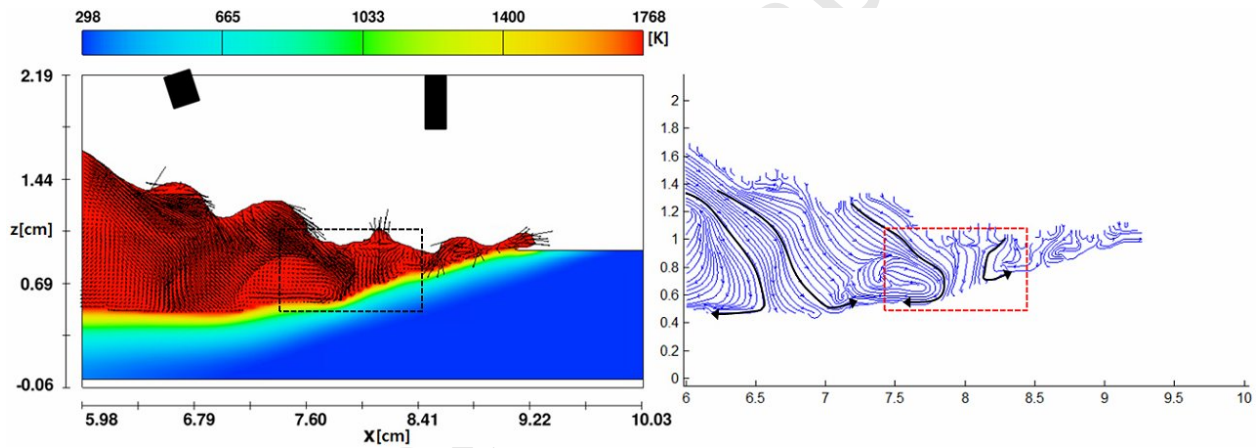
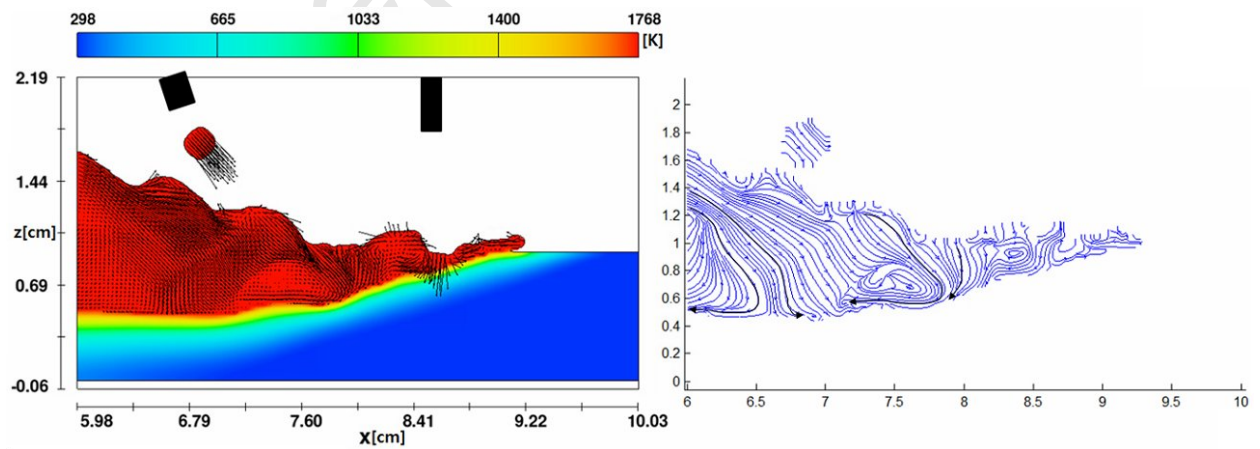
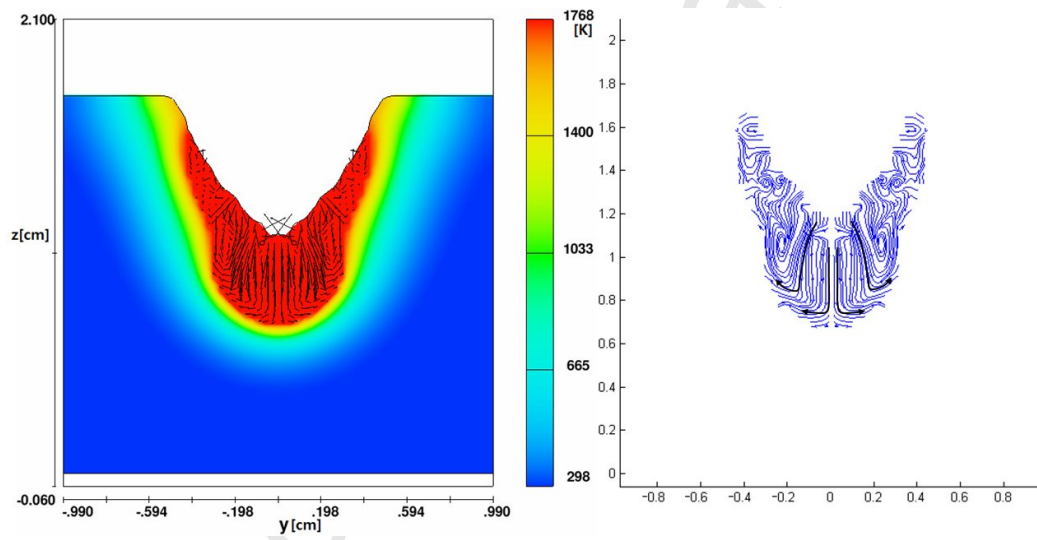
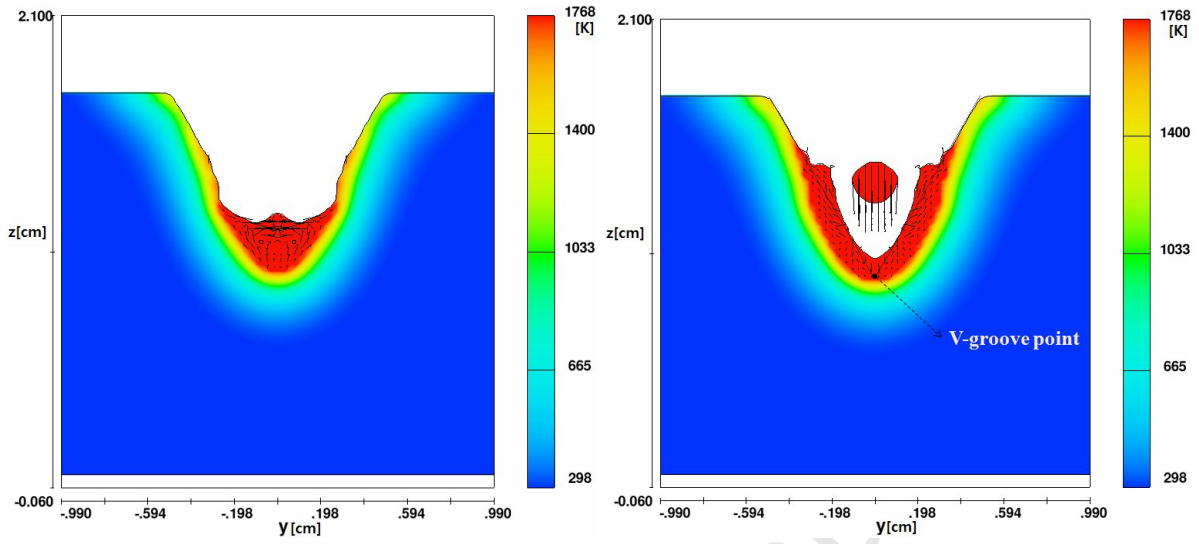


Fig. 8 Calculated temperature profiles and streamlines on the transverse cross sections ($x=44.95mm$) of Case 2

In Case 3, the droplets from the leading electrode fly to forward or backward but the range of the droplet flight is smaller than Case 2; therefore, the volume of the molten pool ahead of the leading electrode in the V-groove is small because the welding speed is very fast and the leading arc forces cover and suppress the molten pool ahead of the leading electrode. In Case 1, the molten pool starts to penetrate under the leading electrode, but in Case 3, a deep penetration is induced between the leading and trailing electrodes due to the fast welding speed. Between two electrodes, the clockwise and counter clockwise molten pool patterns conflict with each other and the resultant molten pool pattern increases the penetration as shown in Fig. 9(b). In the transverse section in Fig. 10, the penetration increases more slowly than in Case 1, and the penetration does not increase although the arc forces and droplet impingement from the trailing electrode are acting on the weld pool. Finally, the penetration of Case 3 is smaller than that of Case 1. However, the molten pool flow patterns from Case 3 form the narrow and deep-penetrated weld bead shape shown in Fig. 13.

(a) $t=2.640\text{s}$ (b) $t=2.644\text{s}$ (c) $t=2.648\text{s}$ **Fig. 9** Calculated temperature profiles and streamlines on a longitudinal cross-sections ($y=0\text{mm}$) of Case 3



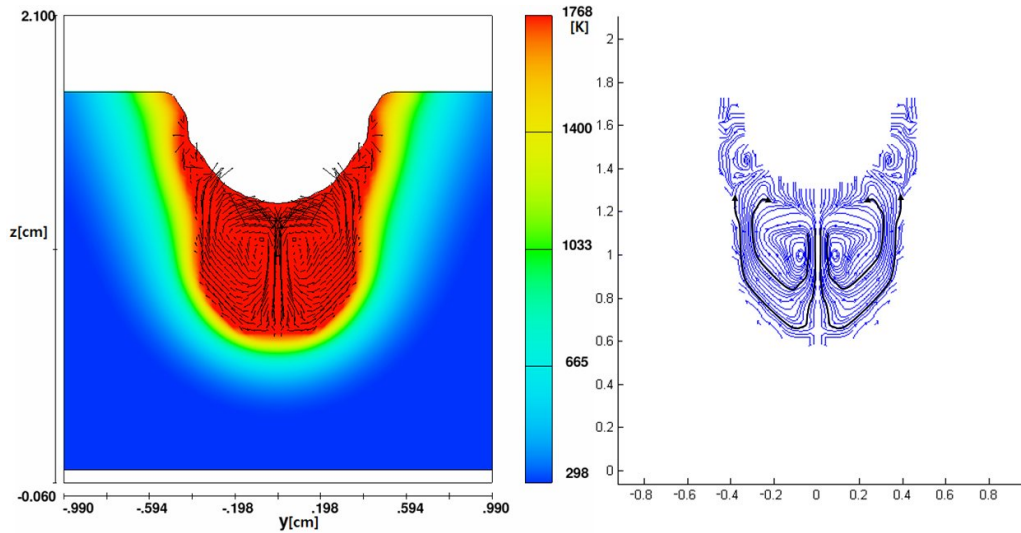
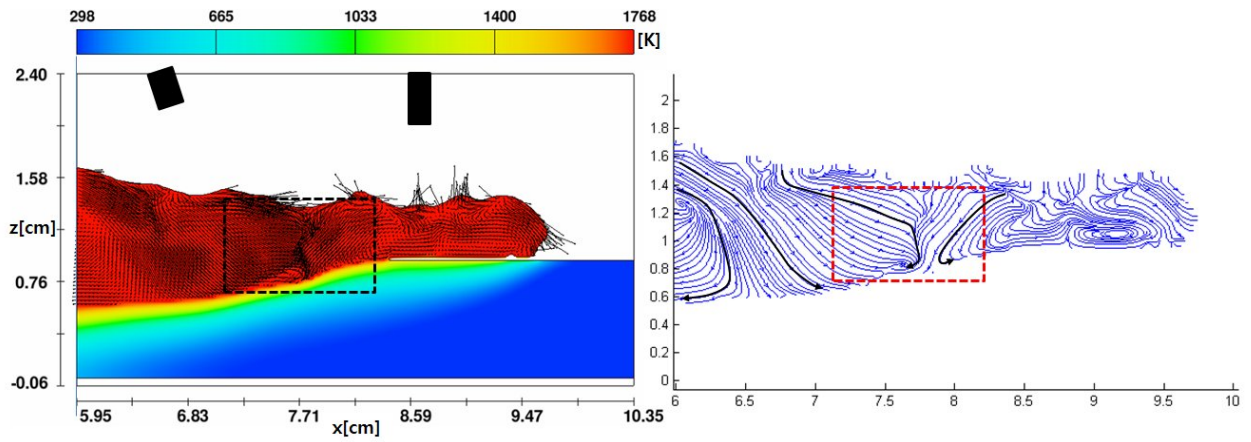
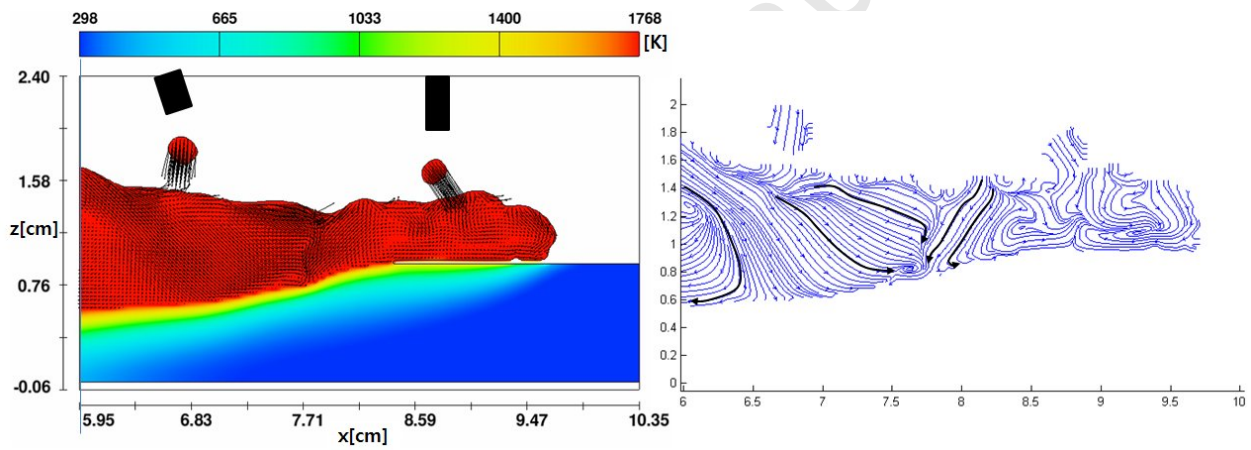
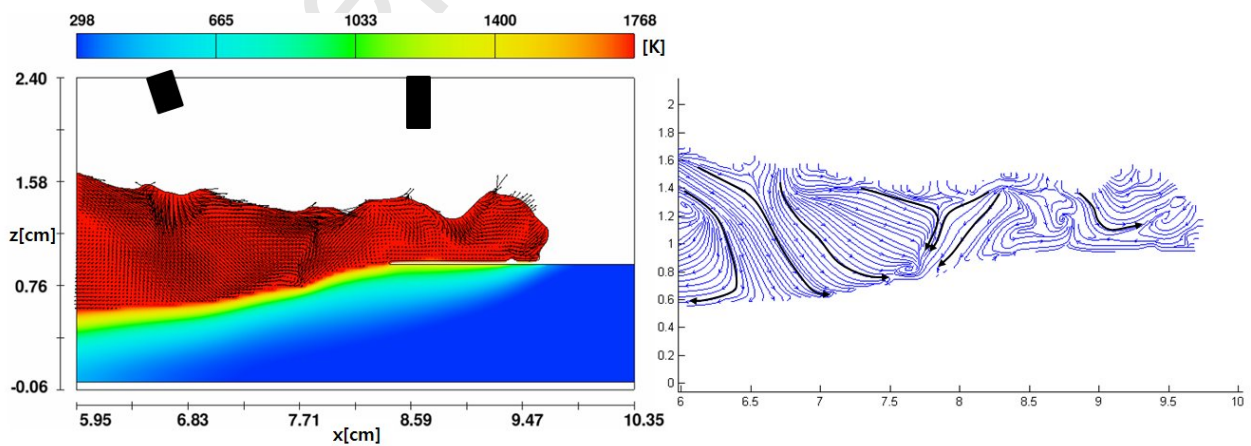
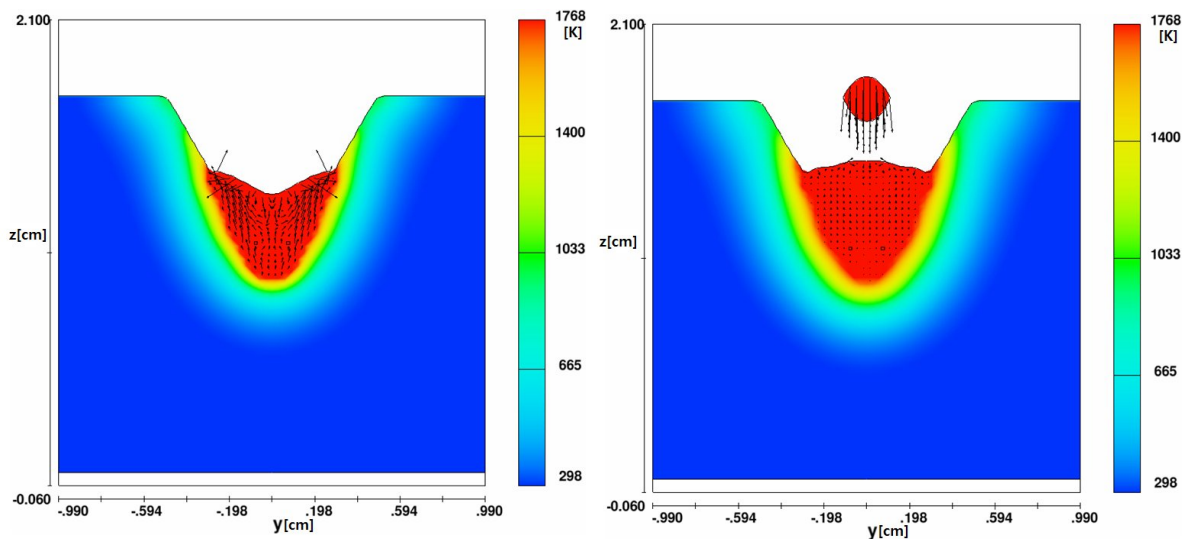
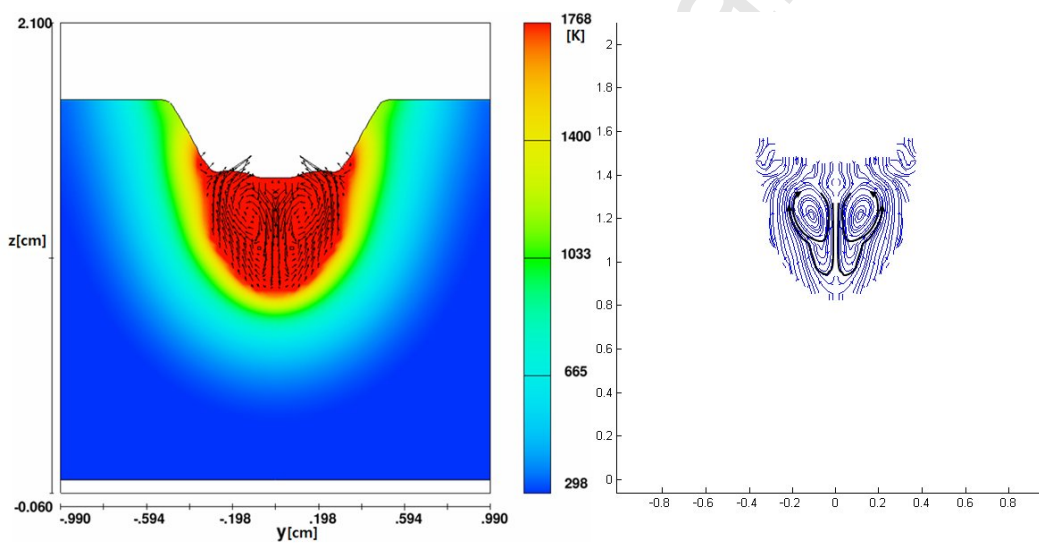
(d) $t=1.680s$

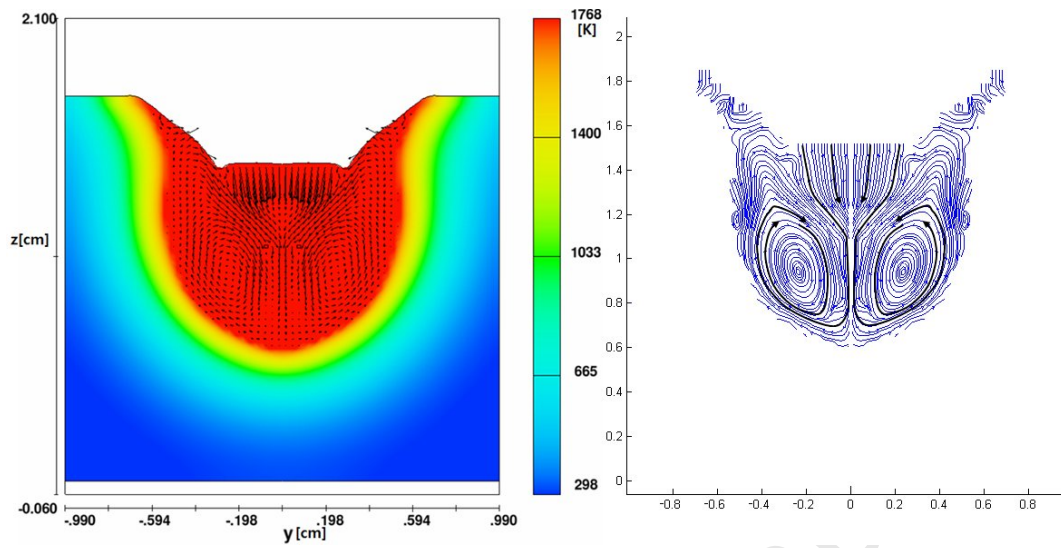
Fig. 10 Calculated temperature profiles and streamlines on the transverse cross sections ($x=44.95mm$) of Case 3

In Case 4, the range of the leading arc center displacement is large so that the volume of the molten pool in the V-groove accumulates ahead of the leading electrode as shown in Fig. 12. Therefore, the molten pool can fill the V-groove even though the leading electrode has not yet approached the spot. As shown in the dotted-box in Fig. 11(a), the clockwise and counter clockwise molten pool conflict with each other, while the molten pool hardly penetrates the weld pool due to the slow droplet speed and the weak arc forces. Finally, a bowl-shaped weld bead is formed as in Fig. 13. However, the area of the fusion zone in Case 4 is smaller than in the other cases due to the highest flux consumption and the resultant smallest arc efficiency.

For all four cases, the trailing arc enlarges the bead width because the voltage of the trailing electrode is higher than that of the leading electrode. Additionally, the resultant bead shapes from the CFD simulation are very similar to the experimental ones in Fig. 13; therefore, the numerical models proposed in this paper are validated.

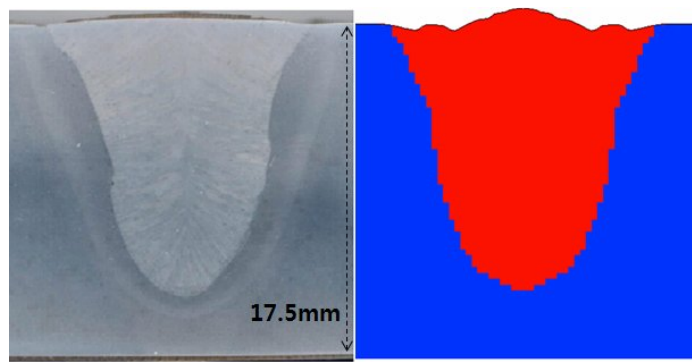
(a) $t=3.782\text{s}$ (b) $t=3.786\text{s}$ (c) $t=3.790\text{s}$ **Fig. 11** Calculated temperature profiles and streamlines on a longitudinal cross-sections ($y=0\text{mm}$) of Case 4

(a) $t=1.437\text{s}$ (before droplet impingement)(b) $t=1.542\text{s}$ (c) $t=2.059\text{s}$

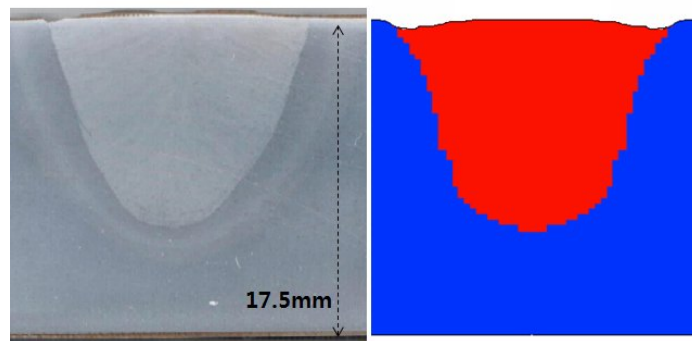


(d) $t=2.922s$

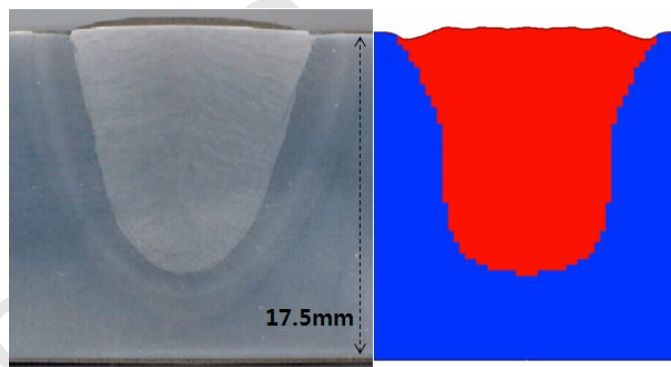
Fig. 12 Calculated temperature profiles and streamlines on the transverse cross sections ($x=44.95mm$) of Case 4



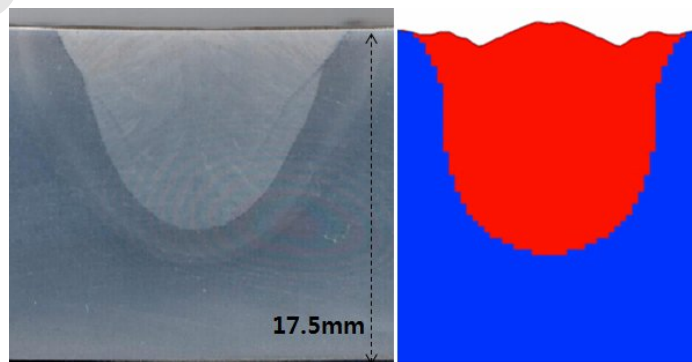
(a) Case 1



(c) Case 2



(c) Case 3



(d) Case 4

Fig. 13 Comparisons of simulation results with experimental ones

5. Conclusions

This paper presented the CFD numerical models and the dynamic molten pool flows in the two-wire SAW-T process.

The results of this work can be summarized as follows:

- (a) The arc interaction effects that consider the arc displacement and the droplet flight are applied to CFD simulations; moreover, the resultant molten pool flow patterns are analyzed.
- (b) The high current in the leading electrode results in the deep penetration weld bead while the small current of the leading electrode results in the relatively shallow penetration due to the accumulated molten pool volume ahead of the leading electrode in the V-groove.
- (c) Even though the same total heat inputs are applied in the two-wire SAW-T process, the resultant bead shapes are different from the combination of current values.

Acknowledgements

The authors gratefully acknowledge the support of the Brain Korea 21 plus project, Korean Ministry of Knowledge Economy (No.2013-10040108) and Mid-career 363 Researcher Program through NRF (2013-015605).

References

- Cao, Z., Yang, Z., Chen, X.L., 2004. Three dimensional simulation of transient GMA weld pool with free surface. *Welding Journal* 6, 169s-176s.
- Cho, D.W., Na, S.J., Cho, M.H., Lee, J.S., 2013a. A study on V-groove GMAW for various welding positions. *Journal of Materials Processing Technology* 213, 1640-1652.
- Cho, D.W., Song, W.H., Cho, M.H., Na, S.J., 2013b. Analysis of submerged arc welding process by three-dimensional computational fluid dynamics simulation. *Journal of Materials Processing Technology* 213, 2278-2291.
- Kiran, D.V., Cho, D.W., Song, W.H., Na, S.J., 2014. Arc behavior in two wire tandem submerged arc welding. *Journal of Materials Processing Technology* 214, 1546-1556.
- Cho, J.H., Na, S.J., 2009. Three dimensional analysis of molten pool in GMA-laser hybrid welding. *Welding Journal* 88, 35s-43s.
- Cho, W.I., Na, S.J., Cho, M.H., Lee, J.S., 2010. Numerical study of alloying element distribution in CO₂ laser-GMA hybrid welding. *Computational Materials Science* 49, 792-800.
- Jaidi, J., Dutta, P., 2001. Modeling of transport phenomenon in a gas metal arc welding process. *Numerical Heat Transfer Part A* 40, 543-562.
- Kim, C.H., Zhang, W., DebRoy, T., 2003. Modeling of temperature field and solidification surface profile during gas metal arc fillet welding. *Journal of Applied Physics* 94, 2667-2679.
- Kim, J.W., Na, S.J., 1995. A study on the effect of contact tube to workpiece distance on weld pool shape in gas metal arc welding. *Welding Journal* 74, 141s-152s.
- Kiran, D.V., Basu, B., Shah, A.K., Mishra, S., De, A., 2010. Probing influence of welding current on weld quality in two wire tandem submerged arc welding of HSLA steel. *Science and Technology of Welding and Joining* 15, 111-116.
- Kiran, D.V., Basu, B., Shah, A.K., Mishra, S., De, A., 2011. Three dimensional heat transfer analysis of two wire tandem submerged arc welding. *ISIJ International* 51, 793-798.
- Kumar, S., Bhaduri, S.C., 1994. Three dimensional finite element modeling of gas metal arc welding. *Metallurgical and Materials Transactions B* 25B, 435-441.

- Mahapatra, M.M., Datta, G.L., Pradhan, B., Mandal, N.R., 2006. Three dimensional finite element analysis to predict the effects of SAW process parameters on temperature distribution and angular distortions in single pass butt joints with top and bottom reinforcements. *International Journal of Pressure Vessels and Piping* 83, 721-729.
- Pardo, E., Weckman, D.C., 1989. Prediction of weld pool and reinforcement dimensions of GMA welds using a finite element method. *Metallurgical Transactions B* 20B, 937-947.
- Shome, M., 2007. Effect of heat-input on austenite grain size in the heat-affected zone of HSLA-100 steel. *Materials Science and Engineering A*. 445, 454-460.
- Tsao, K.C., Wu, C.S., 1988. Fluid flow and heat transfer in GMA weld pools. *Welding Journal* 3, 70s-75s.
- Ushio, M., Wu, C.S., 1997. Mathematical modeling of three dimensional heat and fluid flow in a moving gas metal arc weld pool. *Metallurgical and Materials Transactions B* 28B, 509-+516.
- Wang, Y., Tsai, H.L., 2001. Impingement of filler droplets and weld pool dynamics during gas metal arc welding process. *International Journal of Heat and Mass Transfer* 44, 2067-2080.

List of figures

Fig. 1 Schematic sketch of experimental setup

Fig. 2 Voltage values for all cases in the simulations.

Fig. 3 Current values in the simulations

Fig. 4 Droplet flights due to the arc interaction effects in SAW-T process

Fig. 5 Calculated temperature profiles and streamlines on the longitudinal cross-sections ($y=0\text{mm}$) in Case 1

(a) $t=3.130\text{s}$, (b) $t=3.134\text{s}$, (c) $t=3.138\text{s}$

Fig. 6 Calculated temperature profiles and streamlines on the transverse cross sections ($x=44.95\text{mm}$) of Case 1

(a) $t=1.193\text{s}$ (before droplet impingement), (b) $t=1.281\text{s}$, (c) $t=1.710\text{s}$, (d) $t=1.992\text{s}$

Fig. 7 Calculated temperature profiles and streamlines on the longitudinal cross-sections ($y=0\text{mm}$) of Case 2

(a) $t=3.130\text{s}$, (b) $t=3.134\text{s}$, (c) $t=3.138\text{s}$

Fig. 8 Calculated temperature profiles and streamlines on the transverse cross sections ($x=44.95\text{mm}$) of Case 2

(a) $t=1.257\text{s}$ (before droplet impingement), (b) $t=1.265\text{s}$, (c) $t=1.710\text{s}$, (d) $t=1.992\text{s}$

Fig. 9 Calculated temperature profiles and streamlines on a longitudinal cross-sections ($y=0\text{mm}$) of Case 3

(a) $t=2.640\text{s}$, (b) $t=2.644\text{s}$, (c) $t=2.648\text{s}$

Fig. 10 Calculated temperature profiles and streamlines on the transverse cross sections ($x=44.95\text{mm}$) of Case 3

(a) $t=1.006\text{s}$ (before droplet impingement), (b) $t=1.080\text{s}$, (c) $t=1.442\text{s}$, (d) $t=1.680\text{s}$

Fig. 11 Calculated temperature profiles and streamlines on a longitudinal cross-sections ($y=0\text{mm}$) of Case 4

(a) $t=3.782\text{s}$, (b) $t=3.786\text{s}$, (c) $t=3.790\text{s}$

Fig. 12 Calculated temperature profiles and streamlines on the transverse cross sections ($x=44.95\text{mm}$) of Case 4

(a) $t=1.437\text{s}$ (before droplet impingement), (b) $t=1.542\text{s}$, (c) $t=2.059\text{s}$, (d) $t=2.922\text{s}$

Fig. 13 Comparisons of simulation results with experimental ones (a) Case 1, (b) Case 2, (c) Case 3, (d) Case 4